Nitrogen-doped Oxygen-rich Activated Carbon Derived from Longan Shell for Supercapacitors

Ji Yan[1,2,*], Ya-Yong Fang[1], Shi-Wen Wang[1], Shi-De Wu[2,*], Li-Xia Wang[1], Yong Zhang[1], He-Wei Luo[1], Yang Cao[1], Hai-Li Gao[1], Li-Zhen Wang[2], Fu-Jun Liu[3,*]

[1] School of Materials and Chemical Engineering, Zhengzhou University of Light Industry, Zhengzhou 450001, Henan, PR China
[2] Henan Provincial Key Laboratory of Surface Interface Science, Zhengzhou University of Light Industry, Zhengzhou, 450001, Henan, PR China
[3] Instituto de Fisica, Universidade de Brasilia, 70910-900 Brasilia, DF, Brazil
[*]E-mail: jiyan@zzuli.edu.cn (*Dr. J. Yan*), sdwu@zzuli.edu.cn (*Prof. S.D. Wu*), fliu@unb.br (*Dr. F.J. Liu*).

In this study, longan shell as biowaste material has been collected to prepare activated carbon for supercapacitors. The biochar was firstly carbonized and then etched by KOH to transform into porous carbon architecture. With the help of XRD, SEM, Raman and XPS, physical and chemical properties of the samples were investigated and the optimized parameters of preparation is the etching ratio of 1:2 at pre-carbonization temperature of 500 ^{0}C following the etching temperature at 700^{0}C. Due to the nitrogen-doping carbon combined with oxygen-rich functional groups as well in-situ $CaCO_3$ template, the achieved activated carbon possesses a specific capacitance of 210 F g^{-1} at a current density of 0.5 A g^{-1}, with a moderate rate capability at 20 A g^{-1}. Symmetrical supercapacitor has also been assembled and its power density reaches 17.2 Wh kg^{-1} at energy density of 1, 000 W kg^{-1} with a high capacitance retention of 68.3% from 1 A g^{-1} to 40 A g^{-1}. After tested at 4 A g^{-1} for 10,000 cycles, the capacitor only shows slightly capacitance decay with the retention almost 100%, demonstrating a practical application value in supercapacitors.

1. INTRODUCTION

The ever-increasing global warming crisis has stimulated human society to pursue green energy technology for restricting the emission of carbon dioxide, such as fuel cell, lithium ion battery and so on [1,2]. Bio-resource becomes one of most important branches to substitute the fossil fuel, such as the synthesis of ethanol, the generation of methane or the generation of electricity [3]. Among series practical

application of bio-char, activated carbon derived from bio-waste has gradually attracted enormous attention and exhibits importantly practical application value due to it abundance, environmental benignity and renewability [4]. Supercapacitors based on activated carbon paved a new avenue to reuse bio-waste and gained tremendous research enthusiasm in past decades. For supercapacitor, it usually composes two different energy storage mechanism: electrochemical double-layer capacitance and pseudo-capacitance. When compared with pseudo-capacitor, carbon-based electrochemical double-layer capacitor wins tremendous attention due to its wide raw source, good conductivity, fast charge/discharge rate and stable cycling life. A series of new carbon materials have been prepared and introduced into the supercapacitor-type energy storage devices, such as carbon nanotube [5,6], fullerene [7], graphene [8], and graphdiyne [9].

In spite of diversity of energy storage principle, activated carbon has been widely adopted in assembling asymmetric/symmetric capacitors. However, the research of activated carbon still needs to be paid more attention and the deep understanding of carbon-based composites for supercapacitor is urgent. During the past decades, various activated carbon derived from widespread biomass have been investigated, and adequate energy density/power density has been achieved, such as waste soybean dreg [10], fir bark [11], ant powder [12], bradyrhizobium japonicum [13], corn straws [14], sugarcane bagasse pith [15,16] and so on [17-21]. Among various bio-waste resources, longan shell could be effectively utilized as raw precursor for preparation of environment-friendly carbonaceous electrode materials because they contain oxygen-rich functional groups and nitrogen doping items. Wei [22] attributed the high capacitance of 322 F g^{-1} at 0.5 A g^{-1} current density to the nitrogen-doped porous architecture derived from longan seeds while Luo [23] used longan shell to prepare nitrogen/oxygen co-doped hierarchical porous carbon and treated it as electrode material for sodium ion batteries.

In this work, we find that the existence of $CaCO_3$ is another main reason for constructing the unique architecture when washing with HCl during the synthesis. The combination of such in-situ inorganic template ($CaCO_3$) and KOH etching plays an important role in determining the hierarchical carbon structure from mesoporous to microporous, which not only provides accessible channel for electrolyte penetration and supplies enough reactive surface area for storing electron. When used as the electroactive electrode for supercapacitor, the material exhibits a specific capacitance 210 F g^{-1} at a current density of 0.5 A g^{-1}. Even cycled at a high current density of 40 A g^{-1}, it maintains 68.3% of capacitance retention when compared with that at 1 A g^{-1} and retains almost 100% of capacitance retention after 10,000 cycles at 4 A g^{-1} current density in symmetric supercapacitor.

2. EXPERIMENTAL

The longan shell was washed with distilled water and ethanol several times before drying at 80°C for 24 h. Then, the washed material was crashed into powder and heated at 500°C for 2 h in a tube furnace with flowing nitrogen at 100 sccm. After cooling down to room temperature, the pre-carbonized powder was mixed with KOH at various mass ratio from 1:1, 1:2, to 1:3, respectively. The obtained mixture was well grounded with 20 ml distilled water and then put into a blast oven at 80 °C for 12 h. After the drying treatment, the mixture was reground and further heated in a nitrogen atmosphere in a

tube furnace at 700 °C for 2 h. Then, the obtained product was washed with dilute hydrochloric acid several times and distilled water until the pH reaches 7. For comparison, the samples etched with various KOH mass were denoted as PC-1-1, PC-1-2, and PC-1-3 sample, respectively. The only pre-carbonization powder was named as PC sample.

Microstructures and morphologies of samples were observed by a scanning electron microscopy (SEM, JSM-7100F, JEOL, Japan) and a high-resolution transmission electron microscopy (HRTEM, JEM-2010FEF, JEOL, Japan). Phase structure was characterized by MiniFlex300. Raman spectrum was carried out to analyze graphitization degree of samples by LabRAM XploRA. The chemical composition of the samples was investigated using X-ray photoelectron spectroscope (XPS, ESCALAB 250Xi, Thermo Fisher Scientific, USA).

The working electrode was prepared by blade coating slurry composed of active carbon, super P conductive carbon and polytetrafluoroethylene binder at a ratio of 80:10:10. The electrochemical performance of the activated carbon was investigated by a three-electrode system, wherein the coated electrode was used as a working electrode, platinum plate was used as a counter electrode, and a Hg/HgO electrode was used as a reference electrode, respectively. 6 M KOH solution was utilized as the aqueous electrolyte. The cyclic voltammetry and electrochemical impedance spectra (EIS) were performed by using an electrochemical work station (CHI 660E, Shanghai Chenhua, China), in which the EIS was carried out in a frequency range from 10^5 to 10^{-2} Hz by using an AC voltage with 5 mV amplitude. Galvanostatic charge/discharge test and cycling stability were conducted by using a battery test system (Arbin BT-200, USA) in the potential range of 0-1.0 V. Symmetric supercapacitor was fabricated by using the coated electrode as both cathode and anode with mass loading of ≈4 mg for each electrode. The cathode and anode were pressed together with a porous nonwoven cloth as separator and 6 M KOH solution as electrolyte. The specific capacitance of symmetric supercapacitor can be evaluated on the basis of charge-discharge test together with the following equation:

$$C = \frac{I\Delta t}{\Delta V \times m}$$

Where C is the specific capacitance, I is the discharging current; $\triangle t$ is the discharge time; $\triangle V$ is the potential range during the discharge process after IR drop; and m is the total mass of the two-electrode materials.

Specific energy density and power density are very important performance parameters to determine the practical value of symmetric supercapacitor, which can be defined as follow:
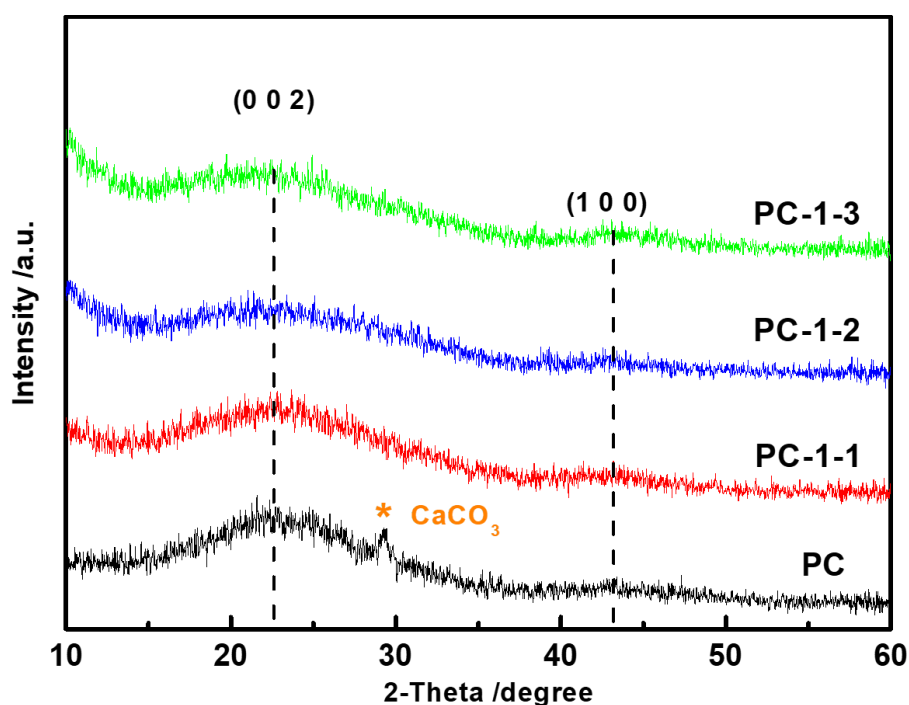
$$E = \frac{CV^2}{7.2}$$

$$P = E \times \frac{3600}{t}$$

Where C is the calculated capacitance, V is the voltage change during the discharge process, E is the energy density, P is the power density, and t is the discharge time. The units of energy density (E) and power density (P) are W h kg^{-1} and W kg^{-1}, respectively.
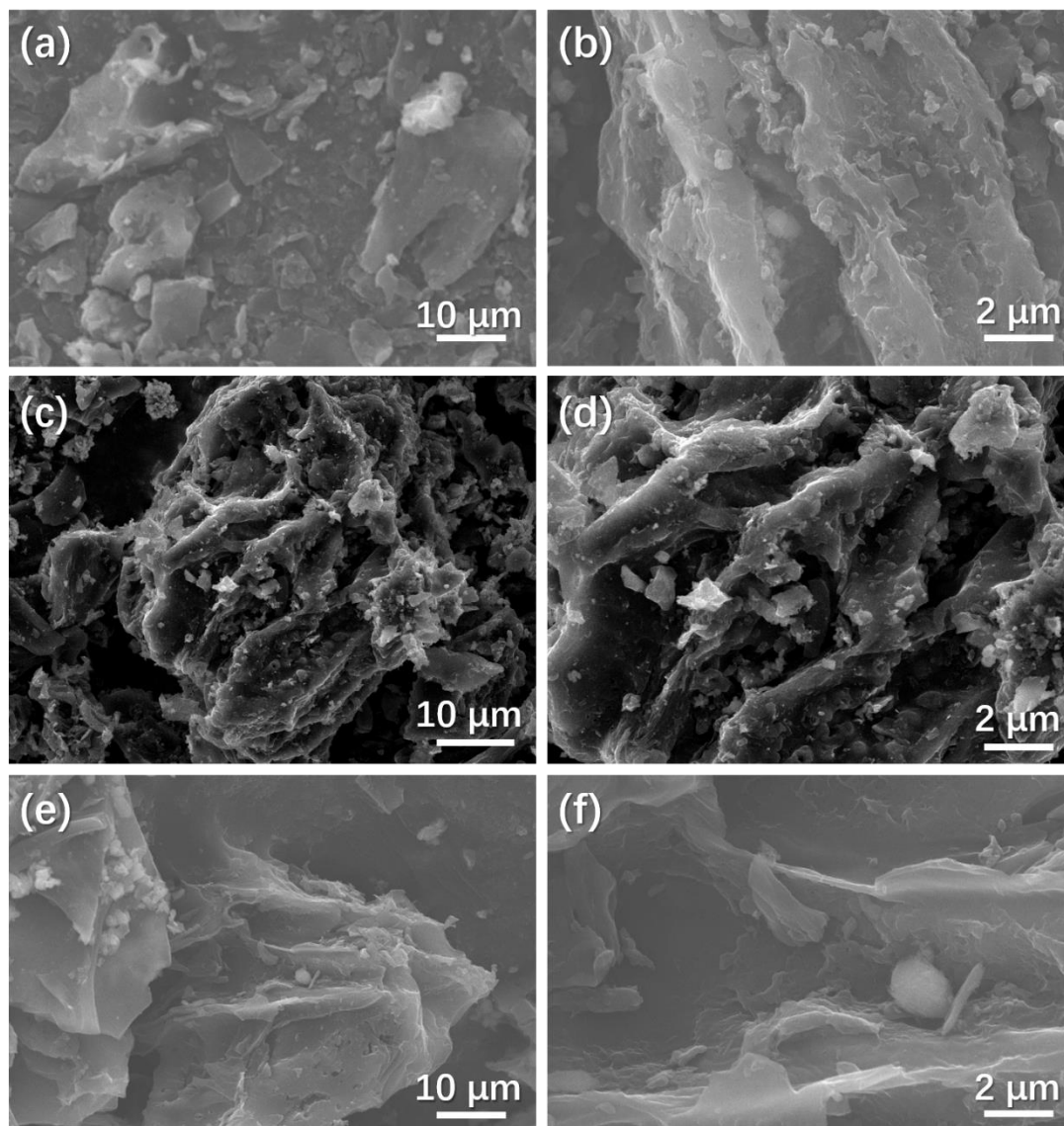
3. RESULTS AND DISCUSSION

The PC samples was synthesized by a simply pre-carbonization treatment of natural abundant longan shell and subsequent etched with 0.5 M KOH solution. The pre-carbonization temperature was fixed at 500 ℃ and the sintering time was set to 2 hours. One interesting phenomenon is that the diffraction peak of $CaCO_3$ (marked at star) is detected from XRD pattern, which clearly demonstrates the existence of in-built template $CaCO_3$. Such inorganic template would facilitate the construction of porous layer-stacking carbon. This observation has not been reported before since the main role of hydrochloric acid was proven to remove the residual KOH. The carbon yield is about 50% as confirmed by calculation the mass of material before/after pre-carbonization.

Figure 1. XRD pattern of PC based samples.

As shown in Figure 1, X-ray diffraction pattern exhibits that a slightly shift of the (002) peak of PC-1-X samples (X=1, 2, 3) towards a lower angle as compared with PC, which means a larger interlayer distance of PC-1-X samples (X=1, 2, 3) and is attributed to the layered architecture with various contents of N and O heteroatoms stemmed from different activation degree [24]. Two broad diffraction peaks at around 23.3° and 43° can be attributed to the (002) and (100) crystal plane diffraction peaks, indicating the low degree of graphitization and amorphous carbon, respectively [25]. The disappearance of $CaCO_3$ diffraction peak after HCl washing further proves the existence of such inorganic template. For PC-1-X samples (X=1, 2, 3), the intensity of (002) peak has shown a slightly decrease with increase the ratio of KOH. The lower intensity from low-angle scatter indicates the high density of carbon after KOH etching. The formed in-situ porous architecture is believed to facilitating the penetration of electrolyte and improving the capacitive performance.

SEM micrographs of the activated carbon before/after KOH etching are depicted in Figure 2. As shown in Figure 2a-2b, the surface of PC-1-1 sample demonstrates irregular bulk shape, which can be attributed inefficient etching by the low usage of KOH. When increase the KOH ratio to 1:2, the material (PC-1-2) is composed of packaged layer nanosheets with relatively hierarchical connected framework. The rough surface has been etched by KOH in some extent. After etched by KOH in 1:3, the activated carbon (PC-1-3) was etched to deeper degree and the hierarchical architecture was destroyed because the excessive ablation of the carbon by KOH. In short, the samples with/without KOH etching manifest irregular blocks and unevenly distributed cavities regardless of the content of KOH activation agent.
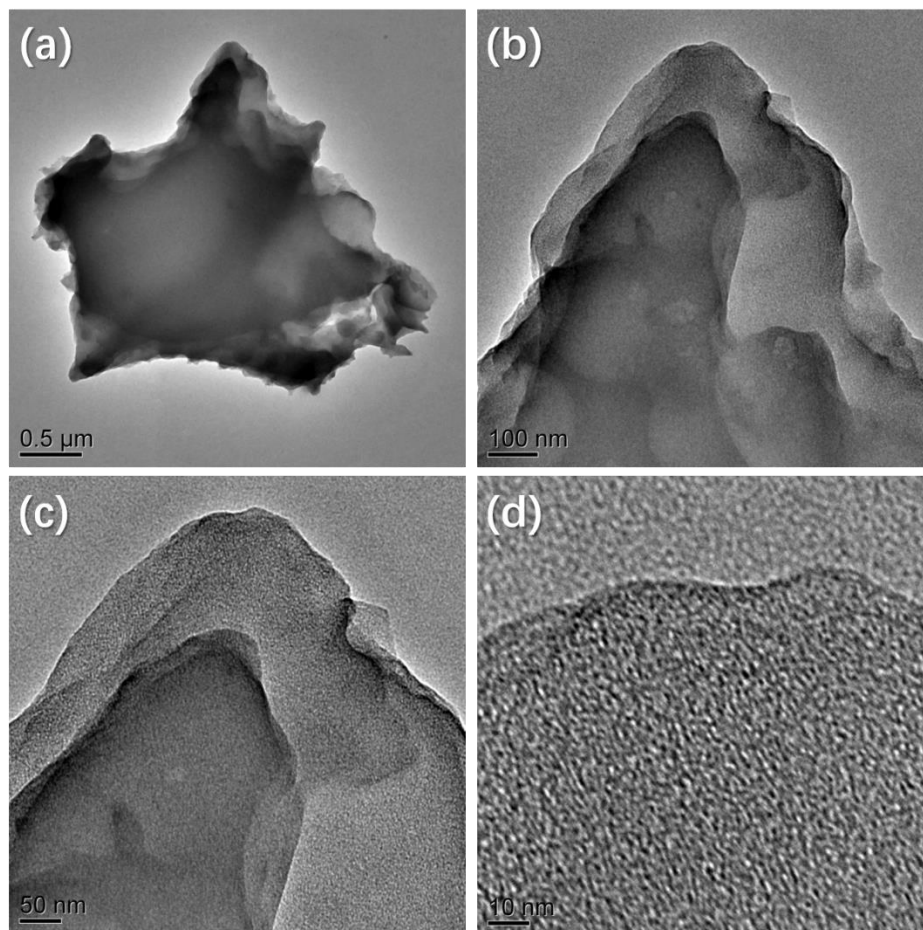

Figure 2. SEM morphologies of PC samples (a-b) PC-1-1, (c-d) PC-1-2 and (e-f) PC-1-3.

Figure 3 shows transmission emission microscope photographs of the PC-1-2 sample. It is easily to be observed that the layer-stacking carbon nanosheets were formed, and there is no detectable lattice

fringe, demonstrating that there is no significant change in the structure for the PC-1-2 sample after KOH etching at 700°C for 2 h.

In order to confirm the altered disorder nature and graphitization of activated carbon with different amounts of KOH, Raman spectroscopic analysis was carried out, and from Figure 4, it is apparent that all three PC-1-X samples (X=1, 2, 3) exhibit two bands at around 1348 cm^{-1} and 1589 cm^{-2}, corresponding to D band and G band, respectively.

Figure 3. TEM images of PC-1-2 sample at different magnification scale.

The D band is related with the disordered carbon structure while the G band is associated with the first-order scattering of the E_{2g} mode of the sp^2 carbon, which indicates the graphitization of carbon [26,27]. As shown in Figure 4, the I_D/I_G of the activated carbon samples gradually increases from 0.97, 0.99 to 1.03 when increasing the KOH ratio from 1:1 to 1:2 and 1:3, respectively, indicating more disordered structure of activated carbon with more usage of KOH, which keeps well consistent with the previous reports [28]. In other words, the higher ratio of KOH, the higher disordered degree of carbon.

The chemical components and types of functional groups of the PC-1-2 sample were further analyzed by XPS. As shown in Figure 5(a), three distinct peaks were detected at binding energy of 284.1, 351.1 and 531.1 eV, assigning to carbon, nitrogen and oxygen atom, respectively. The high-resolution C1s spectrum of the PC-1-2 sample exhibits three peaks in Figure 5(b). The peak at 283.58 eV (C-i) is related to sp^2 hybrid graphite-like carbon while other two peaks at 284.98 eV (C-ii) and 285.98 eV (C-

iii) can be derived from C-N and C-O, respectively [29]. The weaker peaks after 286 eV can correspond to carbonyl, ester or carboxylic groups [14]. In addition, the high-resolution N1s spectrum of the sample was shown in Figure 5(c), from where the peaks at 398.3, 400.1, and 401.2 eV represent pyridinic N (N-i), pyrrolic N (N-ii) and quaternary N (N-iii), respectively [30].
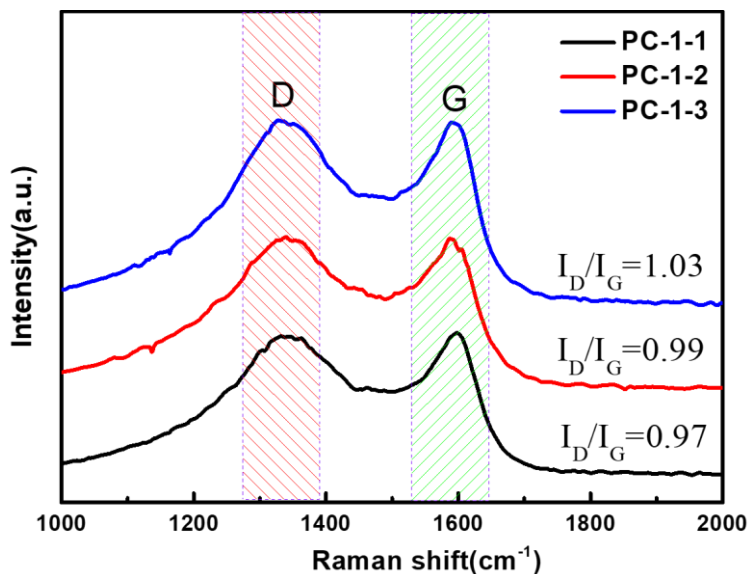

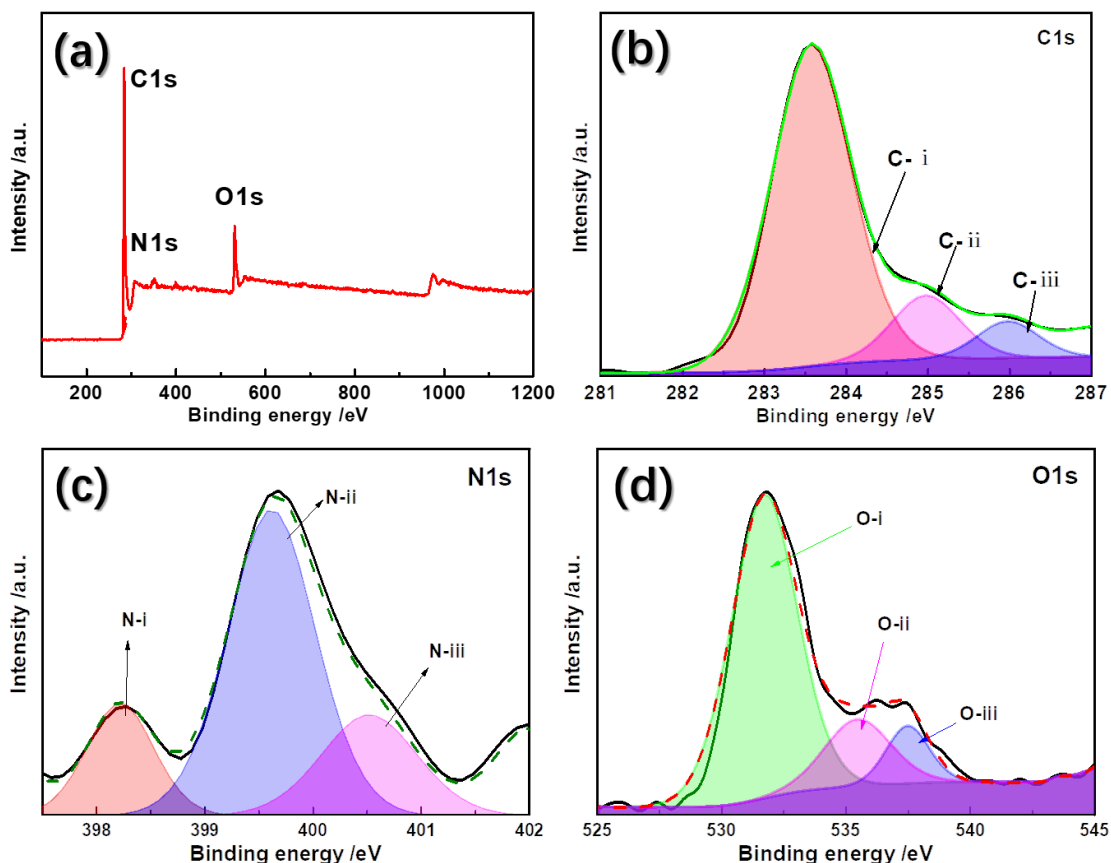**Figure 4.** Raman spectra of PC-1-1, PC-1-2 and PC-1-3 samples.
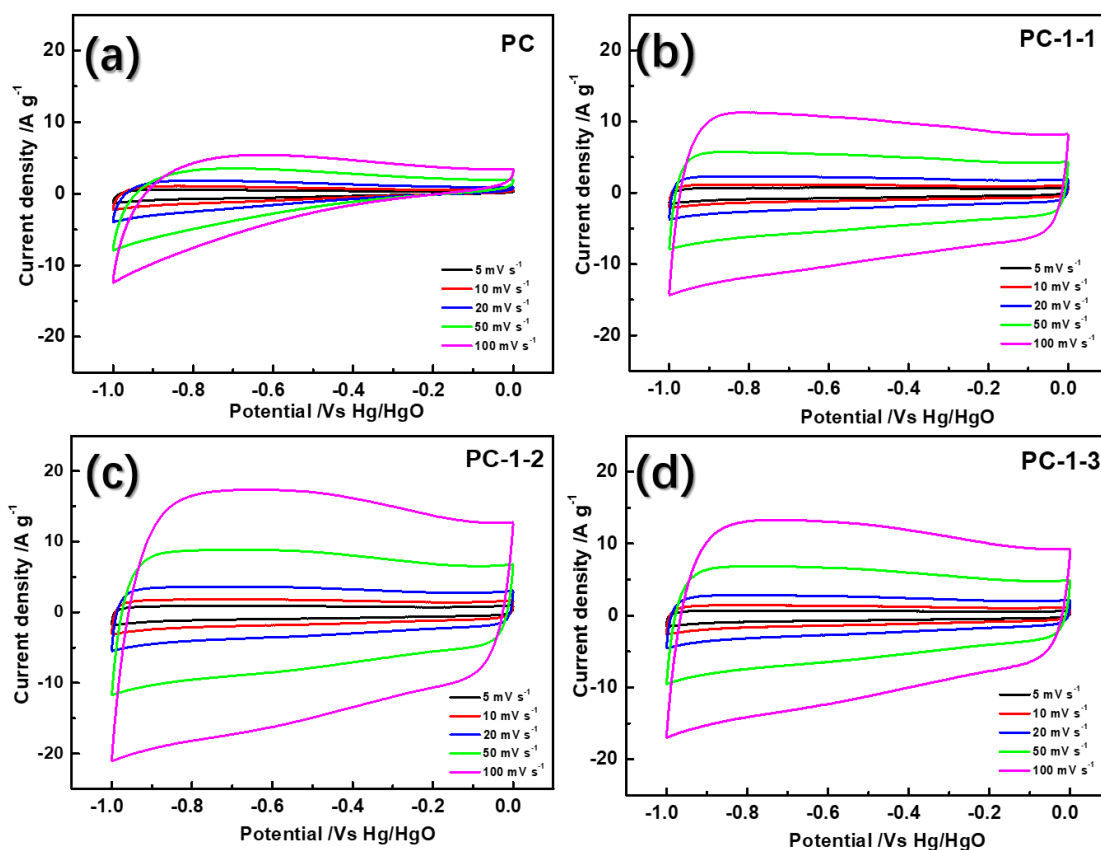

Figure 5. X-ray spectra of PC-1-2 sample (a) full spectrum, (b) C1s, (c) N1s, and (d) O1s.
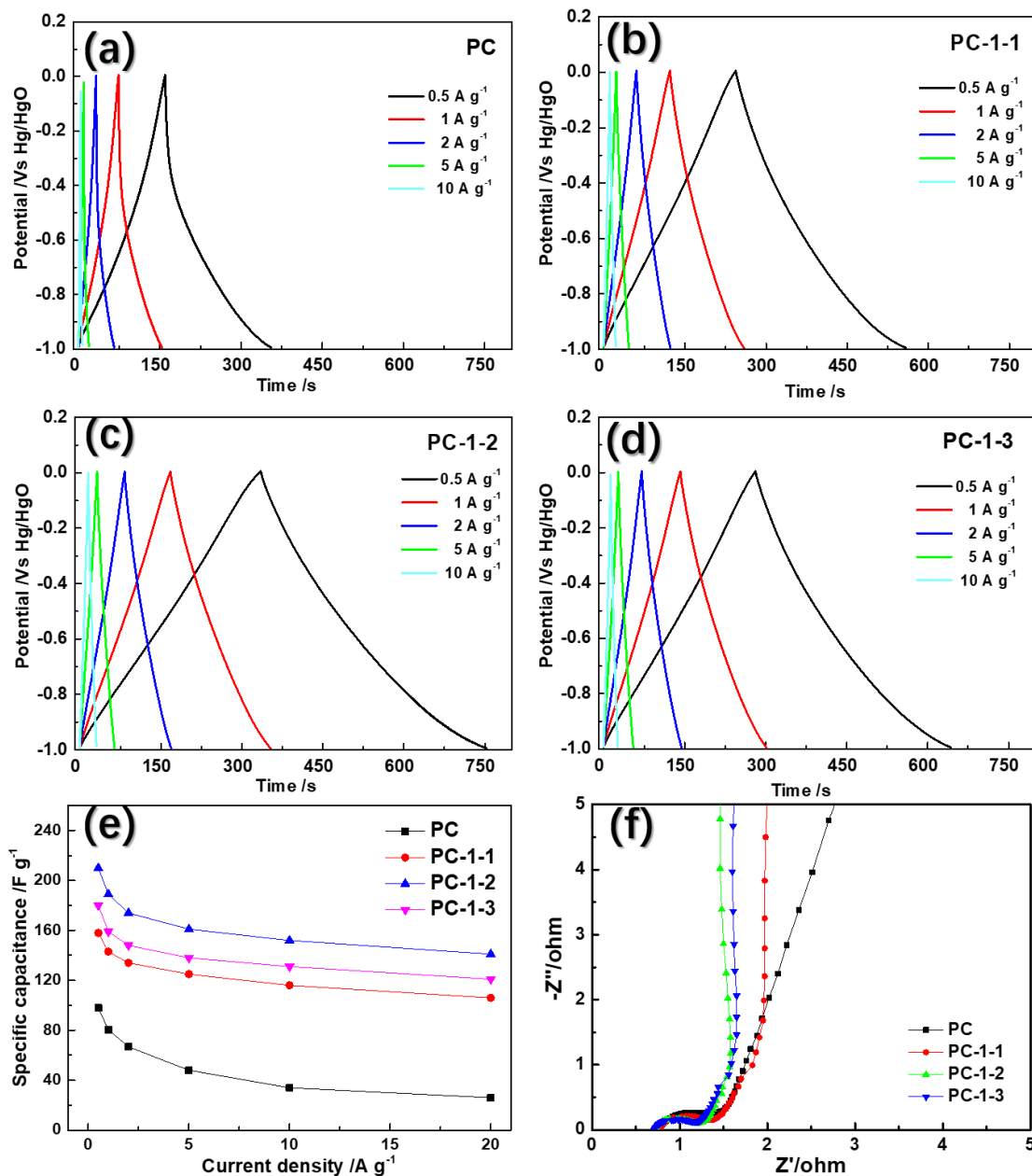
From the high-resolution of O1s spectrum shown in Figure 5(d), there are three representing binding peaks with various contributions located at 531.3, 532.7 and 536.2 eV, ascribing to three types of oxygen functional groups including C=O quinone type group (O-i), C-OH phenolic hydroxyl or C-O-C ether (O-ii), and COOH carboxylic group (O-iii) [31,32]. The existence of these oxygen-based functional groups can ameliorate the surface wettability of carbonaceous material for electrolyte penetration [32], and further suggest the partial graphitization and the oxygen-richer functional groups after KOH etching, which also coincides with the XRD and Raman results.
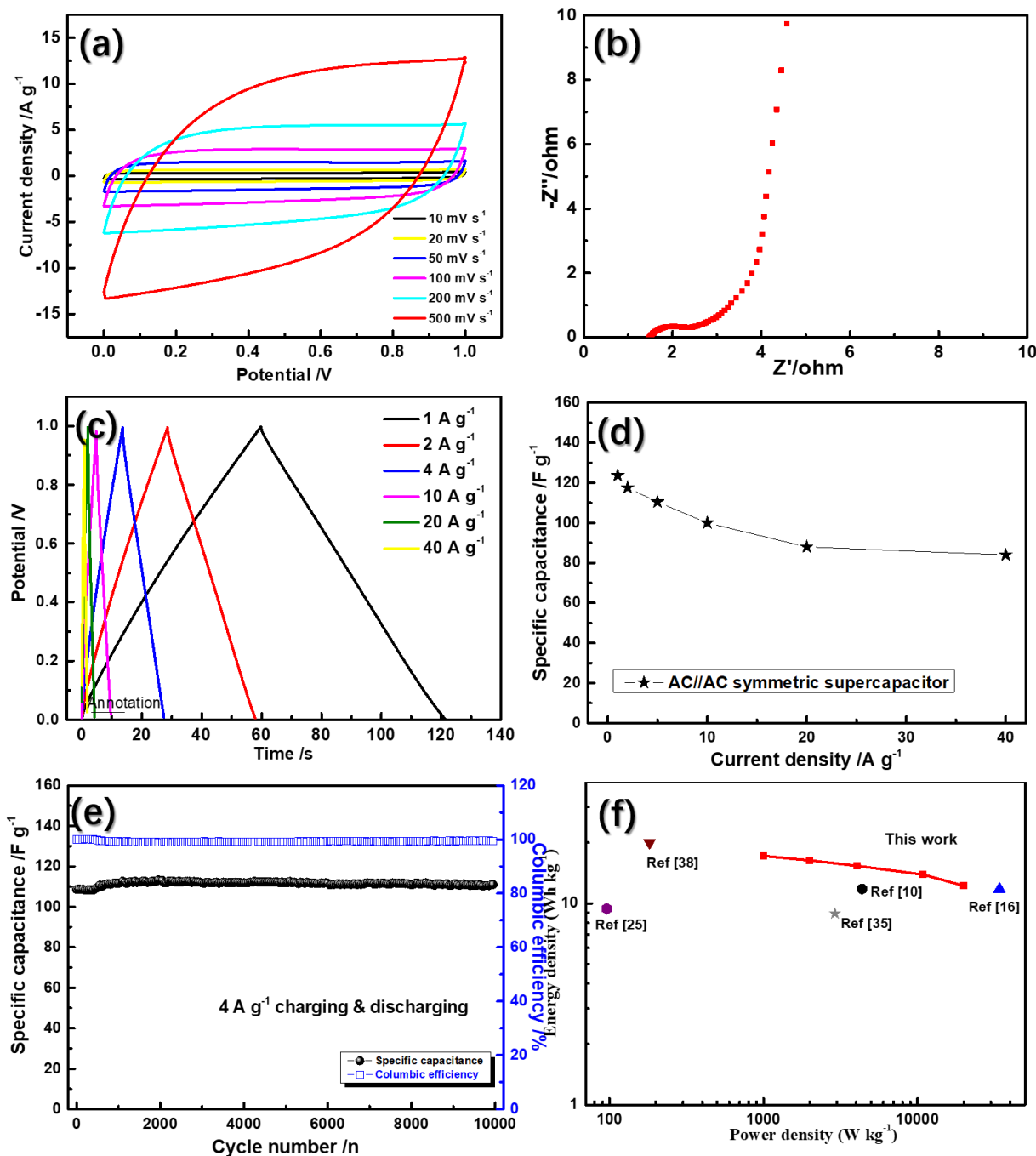

Figure 6. CV curves of (a) PC sample, (b) PC-1-1 sample, (c) PC-1-2 sample and (d) PC-1-3 sample at various scanning rates.

Electrochemical properties of the activated carbon were investigated by using both three-electrode system and two-electrode symmetric capacitor. As shown in Figure 6, the electrochemically capacitive behavior of activated carbon in three-electrode system was investigated by cyclic voltammogram (CV) test. The PC electrode demonstrates a semi-rectangular shape, indicating the main double layer capacitance and limited pseudo-capacitance. The limit current density from the CV curve can be attributed to the only pre-carbonization process at 500°C without any etching or heteroatom doping effect. After etching with different KOH amounts, all CV curves of three PC-1-X samples (X=1,2,3) demonstrate enhanced current density, indicating a significant improvement of double layer capacitance. Among three PC-1-X samples, the PC-1-2 electrode possesses superior electrochemical reversibility when increasing scanning rate from 5, 10, 20, 50 to 100 mV s^{-1}. The well-maintenance of

rectangular shape represents the ideal double layer capacitive behavior, low contact resistance and better rate capability of the electrode [33]. It is noted that a slight distortion of the rectangular shape is observed, and the PC-1-2 electrode shows the higher current density whatever scan rate varies, suggesting PC-1-2 has a higher specific capacitance. This result may be attributed to the introduced heteroatom-based functional groups on the surface of activated carbon rather than specific surface area since there is no significant alteration of surface morphology after KOH etching.

Figure 7. GCD profiles of (a) PC sample, (b) PC-1-1 sample, (c) PC-1-2 sample and (d) PC-1-3 sample at various current densities; (e) Relationship between current density and specific capacitance; (f) EIS spectra of PC samples at discharge state.

Figure 8. (a) CV cures at various scanning rates, (b) EIS spectra at discharge state, (c) GCD profiles at different current densities, (d) Relationship between current densities and specific capacitance, (e) Cycling stability and columbic efficiency, and (f) power density & energy density of the symmetric supercapacitors.

Galvanostatic charge-discharge (GCD) curves of PC sample and PC-1-X samples (X=1, 2, 3) were displayed in Figure 7 (a-d). All four samples exhibit isosceles triangular-like plots, which indicates the excellent capacitive behavior of PC-based supercapacitor. Among four samples, the PC sample delivers specific capacitance of 97.8 F g^{-1}, 80.4 F g^{-1}, 66.8 F g^{-1}, 48 F g^{-1}, 34 F g^{-1} and 26 F g^{-1} at current density of 0.5 A g^{-1}, 1 A g^{-1}, 2 A g^{-1}, 5 A g^{-1}, 10 A g^{-1} and 20 A g^{-1}, respectively. In comparison, the specific capacitance of PC-1-2 sample reaches 210 F g^{-1}, 189 F g^{-1}, 174 F g^{-1}, 161 F g^{-1}, 152 F g^{-1} and

141 F g^{-1}, respectively. The results keep consistent with the CV cures, which means the longer discharging time, the higher specific capacitance. Notably, the specific capacitance of PC-based samples gradually increases with X increasing from 1 to 3 (Figure 7(e)), which can ascribe to rough surface and richer heteroatom-doping content. As well-known, the sufficient rough surface can provide plenty energy storage spaces for accommodating OH$^-$ ions while the heteroatom can further produce functional groups or drawbacks reacting with OH$^-$ ions, providing higher specific capacitance. However, in this manuscript, the etching effect of KOH is not significant as expected. Thus, it is believed that the heteroatom-doping combined with in-situ CaCO$_3$ template may be the main reasons for providing such higher capacitance. In order to further detect the electrochemical information of PC-1-X samples (X=1,2,3), EIS spectra was investigated and the results are shown in Figure 7(f). Although all four samples demonstrate similar semicircle at high frequency region and linear part at low frequency region, Nyquist plots still exhibit slight difference. As we known, vertical curve at the low frequency region always equals to ideal capacitance behavior. The PC-1-2 sample exhibits more vertical plots than that of other three samples, suggesting its ideal capacitance behavior. In addition, the PC-1-2 sample also shows the smallest semicircle at high frequency region, which can be depicted as the relatively low charge transfer resistance and superior electrical conductivity at the electrode/electrolyte interface [34].

Table 1. Comparison of capacitive performance of bio-waste derived carbon materials

Bio-resources	C (F g^{-1})	Rate capability (F g^{-1})	Electrolyte	References
Longan Shell	210 (0.5 A g^{-1})	141 (20 A g^{-1})	6 M KOH	This work
Bamboo shoot shells	209 (0.5 A g^{-1})	188 (10 A g^{-1})	6 M KOH	[35]
Green Tea waste	162 (0.5 A g^{-1})	80 (5 A g^{-1})	1 M H$_2$SO$_4$	[36]
Corn stalk	140 (1 A g^{-1})	-	3 M KOH	[37]
Rice husk	100 (0.1 A g^{-1})	86 (1.0 A g^{-1})	6 M KOH	[38]
Tea waste	167 (1 A g^{-1})	≈140 (20 A g^{-1})	1 M KOH	[39]
Waste wine waste	187 (0.5 A g^{-1})	-	6 M KOH	[40]

The symmetric supercapacitor was assembled to further detect the electrochemical performance of activated carbon. From CV curves (Figure 8(a)), the supercapacitor exhibits ideal rectangular shape even cycled at 200 mV s^{-1} and 500 mV s^{-1} in combining with low charge transfer resistance and vertical plots in EIS plot (Figure 8(b)), suggesting the superior electrochemical reversibility and excellent electric conductivity of the supercapacitor. GCD curves (Figure 8(c)) were investigated to detect the charge-discharge behavior of the symmetric supercapacitor. After carefully calculation, the device demonstrates an initial specific capacitance of 123.6 F g^{-1}, 117.6 F g^{-1}, 110.4 F g^{-1}, 100 F g^{-1}, 88 F g^{-1} and 84 F g^{-1} at 1 A g^{-1}, 2 A g^{-1}, 4 A g^{-1}, 10 A g^{-1}, 20 A g^{-1} and 40 A g^{-1} of current density, respectively, which are higher than that of the state-of-art commercialized supercapacitor system or recent literatures, as shown in Table 1 [35-40]. In comparison with recent literatures about other biomass waste derived activated carbon, the

capacitance from longan shell based carbon is higher or comparable. The improved capacitance may ascribe to the synergistic effect of nitrogen-doping, oxygen-functional groups and in-situ $CaCO_3$ template, which benefits wettability of electrode, increase of pseudo-capacitance and formation of unique architecture.

The capacitance retention reaches 68.3% when the current density increases from 1 A g^{-1} to 40 A g^{-1}, demonstrating a superior cycling stability (Figure 8(d)). In addition, the capacitor could retain a high capacitance of 110.6 F g^{-1} after 10,000 cycles, which corresponds to an almost 100% capacitance retention (Figure 8(e)), which is remarkable when compared with previous studies. Finally, the power density & energy density of the supercapacitor was described in Figure 8(f), and in comparison with recent bio-resource related literatures [10,16,25,35,41], the energy density of the symmetric PC-1-2 reaches as high as 1, 000 W h kg^{-1} at a power density of 17.2 W kg^{-1}. When the power density increases to 20 kW kg^{-1}, the energy density can still retain a value of 12.2 W h kg^{-1}. From the viewpoint of energy and power properties, the symmetric supercapacitor accommodates an enhanced conductivity and excellent cycling stability. The nitrogen doping and oxygen-rich functional groups can be attractive in particular because the rich bonding configurations of the nitrogen atom with the carbon in the lattice, which could contribute P electrons to the device and improve the wettability of electrode without consuming much energy density & power density.

4. CONCLUSION

In summary, densely porous layer-stacking carbon nanosheets were prepared through the carbonization treatment and subsequent etching of longan shell. Due to its richer nitrogen and oxygen functional groups, rough surface morphology, and in-situ $CaCO_3$ formed carbon framework, the longan shell derived activated carbon demonstrates a high energy density, an excellent power density, and a good cycling stability without observable capacitance fade after 10,000 cycles at a current density of 4 A g^{-1}. The reported capacitive performance paves a new avenue for reutilization of such bio-waste in high performance supercapacitors.

References

1. L. Wang, H. Gao, H. Fang, S. Wang and J. Sun, *Int J Hydrogen Energ.*, 41 **(**2016**)** 14864.
2. H. Wang, J. Isobe, D. Matsumura and H. Yoshikawa, *J Solid State Electr.*, 22 **(**2018**)** 2067.
3. J. Wang, P. Nie, B. Ding, S. Dong, X. Hao, H. Dou and X. Zhang, *J Mater Chem A.*, 5 **(**2017**)** 2411.
4. H. Jin, J. Li, Y. Yuan, J. Wang, J. Lu and S. Wang, *Adv Energy Mater.*, 8 **(**2018**)** 1801007.

5.   H. Fang, G. Chen, L. Wang, J. Yan, L. Zhang, K. Gao, Y. Zhang and L. Wang, *RSC Adv.*, 8 **(**2018**)** 38550.

6.   H. Fang, W. Zou, J. Yan, Y. Xing and S. Zhang, *ChemElectroChem.*, 5 (2018) 2458.

7.   S. Zheng, H. Ju and X. Lu, *Adv Energy Mater.*, 5 **(**2015**)** 1500871.

8.   H. Fang, F. Meng, J. Yan, G.-y. Chen, L. Zhang, S. Wu, S. Zhang, L. Wang and Y. Zhang, *RSC Adv.*, 9 **(**2019**)** 20107.

9.   K. Wang, N. Wang, J. He, Z. Yang, X. Shen and C. Huang, *Electrochim Acta.*, 253 **(**2017**)** 506.

10. Y. Zhou, J. Ren, L. Xia, Q. Zheng, J. Liao, E. Long, F. Xie, C. Xu and D. Lin, *Electrochim Acta.*, 284 **(**2018**)** 336.

11. W. Zhao, L. Luo, X. Wu, T. Chen, Z. Li, Z. Zhang, J. Rao and M. Fan, *Wood Sci Technol.*, 53 **(**2018**)** 227.

12. G. Zhao, C. Chen, D. Yu, L. Sun, C. Yang, H. Zhang, Y. Sun, F. Besenbacher and M. Yu, *Nano Energy*, 47 **(**2018**)** 547.

13. Q. Yao, H. Wang, C. Wang, C. Jin and Q. Sun, *ACS Sustai Chem Eng.*, 6 **(**2018**)** 4695.

14. Z. Qiu, Y. Wang, X. Bi, T. Zhou, J. Zhou, J. Zhao, Z. Miao, W. Yi, P. Fu and S. Zhuo, *J Power Sources.*, 376 (2018) 82.

15. K. Gao, S. Zhao, Q. Niu and L. Wang, *RSC Adv.*, 9 (2019) 17358.

16. Q. Niu, K. Gao, Q. Tang, L. Wang, L. Han, H. Fang, Y. Zhang, S. Wang and L. Wang, *Carbon*, 123 **(**2017**)** 290.

17. M. Manoj, C. Muhamed Ashraf, M. Jasna, K. M. Anilkumar, B. Jinisha, V. S. Pradeep and S. Jayalekshmi, *J Colloid Interf Sci.*, 535 **(**2019**)** 287.

18. J. Ren, Y. Zhou, H. Wu, F. Xie, C. Xu and D. Lin, *J Energy Chem.*, 30 **(**2019**)** 121.

19. C. Schneidermann, C. Kensy, P. Otto, S. Oswald, L. Giebeler, D. Leistenschneider, S. Gratz, S. Dorfler, S. Kaskel and L. Borchardt, *ChemSusChem*, 12 **(**2019**)** 310.

20. Z. Song, X. Lu, Q. Hu, J. Ren, W. Zhang, Q. Zheng and D. Lin, *J Power Sources.*, 421 **(**2019**)** 23.

21. Q. Zhu, H. Deng, Q. Su, G. Du, Y. Yu, S. Ma and B. Xu, *Electrochim Acta.*, 293 **(**2019**)** 19.

22. H. Wei, H. Chen, N. Fu, J. Chen, G. Lan, W. Qian, Y. Liu, H. Lin and S. Han, *Electrochim Acta.*, 231 **(**2017**)** 403.

23. D. Luo, P. Han, L. Shi, J. Huang, J. Yu, Y. Lin, J. Du, B. Yang, C. Li, C. Zhu and J. Xu, *App Surf Sci.*, 462 **(**2018**)** 713.

24. Y.-Q. Zhao, M. Lu, P.-Y. Tao, Y.-J. Zhang, X.-T. Gong, Z. Yang, G.-Q. Zhang and H.-L. Li, *J Power Sources.*, 307 (2016) 391.

25. Q. Liang, L. Ye, Z.-H. Huang, Q. Xu, Y. Bai, F. Kang and Q.-H. Yang, *Nanoscale*, 6 (2014) 13831.

26. V. Strauss, K. Marsh, M. D. Kowal, M. El-Kady and R. B. Kaner, *Adv Mater*, 30 (2018) 1704449.

27. J. Yan, R. Tjandra, H. Fang, L.-X. Wang and A. Yu, *Diam Relat Mater.*, 89 (2018) 114.

28. C. Long, X. Chen, L. Jiang, L. Zhi and Z. Fan, *Nano Energy*, 12 (2015) 141.

29. T. Wei, X. Wei, L. Yang, H. Xiao, Y. Gao and H. Li, *J Power Sources.*, 331 (2016) 373.

30. R. J. J. Jansen and H. Van Bekkum, *Carbon*, 33 (1995) 1021.

31. F. Guo, X. Jiang, X. Jia, S. Liang, L. Qian and Z. Rao, *J Electroanal Chem.*, 844 (2019) 105.

32. L. Wan, P. Song, J. Liu, D. Chen, R. Xiao, Y. Zhang, J. Chen, M. Xie and C. Du, *J Power Sources.*, 438 (2019) 227013.

33. J. Liang, J. Zhao, Y. Li, K.-T. Lee, C. Liu, H. Lin, Q. Cheng, Q. Lan, L. Wu, S. Tang, L. An and Y.-C. Cao, *J Taiwan Inst Chem E.*, 81 (2017) 383.

34. H. Zhang, B. Tian, J. Xue, G. Ding, X. Ji and Y. Cao, *RSC Adv,* 9 *(*2019*)* 24682.

35. G. Huang, Y. Wang, T. Zhang, X. Wu and J. Cai, *J Taiwan Inst Chem E.*, 96 **(**2019**)** 672.

36. S. Sankar, A. T. A. Ahmed, A. I. Inamdar, H. Im, Y. B. Im, Y. Lee, D. Y. Kim and S. Lee, *Mater Design.*, 169 **(**2019**)** 107688.

37. K. Yu, H. Zhu, H. Qi and C. Liang, *Diam Relat Mater.*, 88 **(**2018**)** 18.

38. W. Zhang, N. Lin, D. Liu, J. Xu, J. Sha, J. Yin, X. Tan, H. Yang, H. Lu and H. Lin, *Energy*, 128 (2017) 618.

39. X. Song, X. Ma, Y. Li, L. Ding, R. Jiang, *Appl. Surf. Sci.,* 487 (2019) 189.
40. D. Duan, W. Su, X. Tan, F. Hu, Y. Wang, W. Huang, H. Peng, F. Xu, Y. Zou, L. Sun, Int. J. Electrochem. Sci., 14 (2019) 10198.
41. H. Feng, H. Hu, H. Dong, Y. Xiao, Y. Cai, B. Lei, Y. Liu and M. Zheng, *J Power Sources.*, 302 **(**2016**)** 164.